Assessing and modeling the dynamics and persistence of mussels in rocky-shore microhabitats

Romina Vanessa Barbosa[1,2], Cedric Bacher[3], Fred Jean[1], Marion Jaud[4], Jérôme Ammann[4], Yoann Thomas[1,]

[1] Univ Brest, CNRS, IRD, Ifremer, LEMAR, IUEM, F-29280 Plouzané, France
[2] University of Victoria, BC, Canada (current address)
[3] Ifremer, DYNECO, F-29280 Plouzané, France
[4] Univ Brest, CNRS, Ifremer, Geo-Ocean, IUEM, F-29280 Plouzané, France

Corresponding Author:
Romina V. Barbosa
Email address: rominavanessa.barbosa@gmail.com

ORCIDs

Romina V. Barbosa: 0000-0003-1793-8444

Marion Jaud: 0000-0002-7629-9710

Cédric Bacher: 0000-0001-6090-4667

Fred Jean : 0000-0002-1132-230X

Yoann Thomas: 0000-0001-7980-5239

Jerome Ammann : 0000-0002-2574-9849

Keywords: Species distribution, intertidal height, disturbance, resilience, remote sensing, Markov chain model.

Abstract

In intertidal rocky shores, sessile organisms are subject to local variations due to a complex interplay of physical and biological drivers. Here, we examined the patterns and the dynamics of distribution of a key benthic ecosystem-engineer species, the mussel *Mytilus galloprovincialis*. We characterized areas of loss, gain, and persistence of mussel space occupancy using drone images with a resolution of one centimeter across two rocky shores spanning 3121 m^2 and 3499 m^2. Then, we assessed the effect of microhabitat slope, microhabitat orientation, and intertidal height on the dynamics of mussel distribution for the two rocky shores. Notably, substantial losses were observed, ranging from 55% to 80% depending on the shore. The hierarchical impact of habitat topographic features on mussel occupancy dynamics diminishes in the order of rocky shore, intertidal height, and microhabitat features. To unravel the dynamics further, we calculated persistence, resilience, and the time to recover from disturbance using a Markov Chain model. Persistence time decreased at the extremes of the rocky shore —both its top and bottom edges. Contrary to expectations, mussels at these edges exhibit higher resilience, preventing their disappearance despite significant losses. Our results not only provide insights into the structural dynamics but also emphasize the need to consider long-term responses to environmental changes. This study underscores the potential of integrating models with drone technology for monitoring intertidal populations, offering a powerful tool to comprehend and anticipate the enduring impacts of environmental shifts on spatial distribution.

Introduction

Understanding and predicting changes or the persistence of species distribution are major goals in population ecology related to important issues (Silliman et al. 2011, Wootton & Forester 2013). In marine ecosystems, the persistence and changes in the distribution of species are generally addressed at high spatial scales where major drivers, such as those related to climate change, modify species occurrence and geographical boundaries (Poloczanska et al. 2013, Thomas et al. 2020, Curd et al. 2023). However, the interaction processes between organisms and their environment take place first at individual level (i.e., ecophysiological processes) and thus on a small scale. This likely has repercussions on species distribution dynamics that may be contradictory to large-scale trends due to local conditions that do not necessarily follow large-scale trends (Helmuth 2002).

In intertidal rocky shores, sessile organisms are subject to local variations due to a complex interplay of physical and biological drivers, such as microclimate temperature and small-scale topographic features and interspecific competition (Dayton 1971, Seabra et al. 2011, Meager et al. 2011, Choi et al. 2019). For instance, Meager et al. (2011) showed that topographic features and temperature influence the abundance and body-size distribution of invertebrates on a rocky shore. The relationship between environmental conditions and the spatial distribution of species seems evident, although the particular role of each factor and the

driving mechanisms is complex and not well understood (e.g., Barbosa et al., 2021). In these habitats, mussels are sentinel species studied to understand the effect of environmental conditions on species' dynamics and distribution (Helmuth et al. 2011, 2016). Mussels are one of the dominant species inhabiting the mid-intertidal zone of temperate rocky shores worldwide (Paine 1974, Paine & Levin 1981) and are considered paramount ecosystem engineers (Borthagaray & Carranza 2007, Arribas et al. 2014). The dynamics and persistence of these ecosystem engineer species are of main interest because their presence increases biodiversity (Arribas et al. 2014, Scrosati et al. 2021), and, thus, changes in their distribution can produce cascading effects on community structure and productivity (Silliman et al. 2011).

Merging field observations and models allows the simplification of complex systems by integrating the multiple processes involved in the dynamics of species distribution. Such integration provides the tools to understand spatial and temporal changes, as well as to test hypotheses (Guichard et al. 2001, Wootton 2001). The development of high-resolution spatial analysis from aerial images has allowed the mapping of intertidal species distribution with high accuracy and detail (Guichard et al. 2000, Gomes et al. 2018, Garza 2019, Barbosa et al. 2022), and could help to understand its long-term dynamics. The majority of studies on mussel distribution dynamics focus on observations of recovery after experimental disturbance, such as in-situ removal of mussels in a specific square area (e.g., Carrington et al., 2009; Guichard et al., 2003). Hunt and Scheibling (2001) studied natural disturbance in two rocky shores, but their conclusions were based on the entire area rather than on the microhabitat scale. Studying the distribution dynamics using drone images would not only allow to map entire rocky shores but also to determine the spatial patterns among microhabitats. Combining observations and models has been successfully applied to assess the colonization process or successions between species (Wootton 2001, Guichard et al. 2003). Markov chain approach is based on probabilities of transitions between different states, e.g., the probability of transition from an occupied to an empty state and vice versa. Among other advantages, Markov chains allow the assessment of the equilibrium state and estimate the time needed to reach this equilibrium after a disturbance, and offer the prospect of a change in scale (Hill et al. 2002). Experimentally tractable local scales can be scaled up to recreate larger-scale patterns (Wootton 2001, Guichard et al. 2003).

In a previous study, drone images were used to map mussel distribution (Barbosa et al. 2022). Results showed that distribution of mussels was primarily related to the intertidal height gradient and, to a lesser extent, to habitat morphology in slope and orientation (Barbosa et al. 2022, see also Gilek et al. 2001). Based on that pattern, we hypothesized that the persistence of mussel aggregations determines higher occupancy at intermediate intertidal heights.

According to this hypothesis, the proportion of occupied area (relative to the available area) would increase if mussels persist over time. In contrast, the top and bottom intertidal boundaries should present a higher probability of loss with a consequent decrease in occupancy. Similarly, we hypothesized that the topographic microhabitat conditions, slope, and orientation, are related, but to a lesser extent, to mussel dynamics.

Here, we used both mapping (drone surveys) and modeling (Markov chain modeling) to assess the effect of microhabitat features on the dynamics of the distribution of a benthic intertidal mussel, *Mytilus galloprovincialis*, and to estimate key properties of the temporal dynamics of mussel distribution. We studied two rocky shores of the same bay as a natural laboratory where the general oceanographic conditions affect microhabitats similarly within both shores but differ depending on the shore orientations (mesoscale). Specifically, we evaluated the effect of shore and microhabitat intertidal height, slope, and orientation angle on the mid-term (annual changes) dynamics of *M. galloprovincialis* distribution. We also assessed the long-term effect of intertidal height on the persistence and resilience of the population, as well as the potential role of disturbance on the species' occupancy pattern along the intertidal height gradient. To do that, we 1) evaluated the temporal dynamics of the distribution (loss, persistence, and gain) of mussel aggregations during a period of a year from drone images, 2) related the observed dynamics with the microhabitat intertidal height, slope, and orientation angle, and 3) modeled the long-term dynamics of lost and gained areas to estimate their long-term persistence, resilience capacity, and time to return to equilibrium after a disturbance.

Methods

Study site

The study was conducted at "Le Petit Minou" site, located on the western coast of French Brittany, France (Fig. 1A). This site is characterized by a macrotidal regime at the entrance of the Bay of Brest. The site comprises two rocky shores on both sides of a sandy beach, here referred to as the West and East shores based on their positions. The West shore is oriented to the south-southeast, whereas the East shore is oriented to the west (Fig. 1B). The West and East rocky shores encompass a total available intertidal area within the mussel distribution range (3.32–5.80 m) of 3121 m^2 and 3499 m^2, respectively (Barbosa et al. 2022).

"Le Petit Minou" site has been characterized by a dominance of *Mytilus galloprovincialis* (Simon et al. 2020), although hybrid individuals are common in the Brittany region (Bierne et al. 2003). The mussel structure is mainly compound by monolayer aggregations in both rocky shores (Barbosa et al. 2021).

Drone image acquisition and processing

Drone surveys were performed on two dates, June 5, 2019, and June 23, 2020, on each of the two rocky shores. Images were processed to construct the digital surface model (DSM) and orthomosaics of both rocky shores and dates using PhotoScan v.1.4.0 software (Agisoft LLC, St. Petersburg, Russia, currently known as Metashape). We employed the Time-SIFT approach (Feurer & Vinatier 2018), which involves aligning all images from different periods (specifically, June 2019 and June 2020) and then separating the previously aligned images for each date to create 3D dense point clouds and generate the SDM and orthomosaic. This process ensured perfect alignment between the orthomosaics of both dates, facilitating a more precise evaluation of temporal changes (Feurer & Vinatier 2018). Due to the high number of cells in the resultant layer (cell resolution 0.5 x 0.5 cm) and the difficulty of processing the total ~16M cells/rows, we resampled the layer at a cell resolution of 1 x 1 cm in QGis v.3.14.16 (QGis Development Team, 2020) for further analyses. Subsequently, we identified changes at each cell of the orthomosaic, i.e., at a centimeter resolution.

Identification of mussels' distribution on two dates

The identification of mussels was carried out by calculating the Mussel Visualization Index (MVI) from the orthomosaics (Barbosa et al. 2022).

$$\text{MVI} = \left(B - \frac{(R+G)}{2}\right)100$$

where B represents blue, R represents red and G represents green, the three bands (RGB) of each cell (pixel) in the orthomosaics. Then, we applied a date- and site-specific threshold to differentiate mussels from other species and substrates based on manually sampled pixels of mussels and non-mussel areas from the constructed orthomosaic (details in Barbosa et al. 2022).

Areas with the presence of algae and lichens in the bottom and upper intertidal height (outside the mussel range) as well as some shadow areas exhibited similar MVI values to mussel areas. To enhance mussel identification, we performed the following workflow: 1) mask by hill-shade distribution, 2) identify mussel intertidal height range, 3) select site's cells within mussels' MVI range, and 4) select mussels' cells by intertidal height range (after Barbosa et al. 2022). This workflow was applied for each date, with the dataset and analyses from June 2019 identical to those presented in Barbosa et al. (2022). The intertidal height range of mussel distribution in the study site was recorded as between 3.2 to 5.80 m above the Lowest Astronomical Tide (LAT) in 2019 (Barbosa et al. 2022). Cells outside this range were considered false positives (false mussel coverage cells) and discarded from both orthomosaics (2019 and 2020).

The accuracy of the resultant distribution dynamics was assessed by sampling 130 cells from each orthomosaic (total of 520 cells; 130 cells x 2 rocky shores x 2 dates). For each orthomosaic, 30 cells corresponded to mussels and 100 to non-mussel cells. Non-mussel cells were manually selected from the orthomosaic, where high resolution allowed unequivocal visual differentiation of mussels from the substrate or other species' cells. Mussels' cells were also manually selected to represent the wide spatial distribution of mussels. Mussels and non-mussels' reference cells were compared with the result of the mussel identification process in a confusion matrix. The confusion matrix presents the proportion of cells corresponding to mussels and non-mussels' cells that were correctly identified, as well as the proportion that was erroneously classified. Then, the overall accuracy (Congalton 1991) and the Kappa index (Kruskal & Wallis 1952, Cohen 1960), were used to determine the accuracy of the supervised classification. Overall accuracy represented the percentage of cells correctly classified, whereas the Kappa index represented the concordance between the supervised classification and the real distribution of mussels. The Kappa index can take values from -1 to 1, with -1 equivalent to zero, whereas 1 indicates perfect concordance (true positives and true negatives).

Characterization of the dynamics of mussel's occupied area

The temporal dynamics of mussel distribution were derived by comparing both orthomosaics, from June 2019 and June 2020, to create a layer with three categories: 'persistence', gain' and 'loss'. Areas initially covered in 2019 that continued to be occupied in 2020 were classified as 'persistence areas'. Areas initially covered in 2019 that showed an absence of mussels in 2020 were classified as 'lost areas', and areas with an initial absence of mussels that were occupied in 2020 were classified as 'gained areas'.

To characterize the distribution dynamics, we initially measured the net area of persistence, gain and loss on each rocky shore, calculating their proportions relative to the entire shore. Additionally, we computed the probability of loss, gain and persistence along the intertidal height range on both rocky shores. Loss probability was defined as the ratio of occupied cells in 2019 that became empty in 2020; Persistence probability as the ratio of occupied cells in 2019 that remained occupied in 2020; and, Gain probability as the ratio of empty cells in 2019 that became occupied in 2020. Probabilities were averaged at 20 cm intervals along the intertidal zone occupied by mussels, ranging from 3.2 to 5.8 m above the LAT (Barbosa et al. 2022).

Furthermore, we determined the probability of loss, persistence, and gain for each topographic microhabitat (intertidal height-slope-orientation). To achieve this, we aggregated cells (from the distribution dynamics layer) with similar microhabitat features, i.e., intertidal height, slope and orientation, and calculated loss, persistence, and gain probabilities as indicated above. The slope was classified into five ranges, each spanning 10 degrees from 0 to 60 each. Similarly, the orientation was divided from 0 to 360 every 30 degrees (counterclockwise, with 0 representing North). We created a merged dataset containing mussel distribution dynamics and topographic features corresponding to each cell in the orthomosaic. To achieve this, the distribution dynamics layer was converted from raster to points, and this point layer was used to extract information from layers of topography (DSM), slope, and orientation (at a resolution of 20 x 20 cm). Topographic feature layers were downscaled from 1 to 20 cm resolution to facilitate processing across the entire study area and avoid very localized roughness effects.

To identify the main features related to observed mussel distribution dynamics, we evaluated the amount of variance explained by each feature and their potential interactions using the linear models function in R. We calculated the variance explained using the

proportion of the total variation explained by a variable, denoted as η^2 (Lane, Online Statistics Education).

$$\eta^2 = SSQ_{effect} / SSQ_{total}$$

where SSQ_{effect} is the sum of squares due to an effect or factor, and SSQ_{total} is the total sum of squares. It is important to note that we used the model fit to extract the calculated sum of squares, not to test for the statistical significance of the factors. The proportion of the total variation explained by each variable (η^2) was represented as a percentage in a Venn diagram for loss, persistence, and gain from each shore. Intertidal height was treated as a continuous variable represented by ranges of 20 cm along the intertidal zone occupied by mussels. The slope and orientation topographic features (independent variables) were treated as categorical variables with several levels determined by a range of values. Cells with a slope higher than 60 were excluded from the analyses due to their low representation (few cells and lack of representation of all orientation angles) in the study area. The entire process of extracting layer information and creating the complete dataset was performed in R (R Core Team, 2020) using raster package functions (Hijmans 2020).

Model of the dynamics of mussel's occupied area

The model represents the dynamics of a theoretical cell defined as a square area of 1 cm^2, which is the same scale of observations made at a given intertidal height position on a single shore. Cells occupied by mussels may become empty due to disturbances, such as dislodgement or mortality, related to the effect of external factors. Each cell can be in two ecological states, depending on the presence (*Occupied*) or absence (*Empty*) of mussels (Fig. 2A). An *Occupied* cell has a probability to stay occupied for one more year (persistence probability, denoted as *p*). Each *Occupied* cell may also become *Empty* with a loss probability *1-p*. The probability of change from *Empty* to *Occupied* between two consecutive years is defined as the gain probability *q* (Fig. 2A).

Markov chain theory predicts that the proportions of cells in *Occupied* vs *Empty* states reach equilibrium, remaining constant over time (Wootton, 2004; Fig. 2B). Consequently, mussel distribution is expected to fluctuate annually due to disturbances, while the proportions of *Occupied* vs *Empty* cells remain stable unless additional disturbances occur. The main calculations are as follows (refer to Supplementary 2 for mathematical proof):

- the proportion of *Empty* cells is $\mu = \frac{1-p}{1-p+q}$

- the proportion of *Occupied* cells is $\lambda = \frac{q}{1-p+q}$
- the *Gained* cells result from the changes from *Empty* to *Occupied* states and are equal to $q.\frac{1-p}{1-p+q}$. At equilibrium, the proportion of *Gained* cells equals the proportion of *Lost* cells, thus, there is no absolute lost or gained area since they cancel each other.

The model properties allowed us to derive important features characterizing the population's long-term dynamics, such as (refer to Supplementary 2 for explanations and mathematical proofs):

- the persistence time, defined as the maximum time during which 90 % of *Occupied* cells remain occupied (90th percentile) in the absence of disturbance, is equal to: $a = \frac{log(0.1)}{log(p)}$
- the resilience index, a metric of the capacity to return to equilibrium after a disturbance (loss event), is equal to $r = 1 - |q - p|$. This indicator ranges between 0 and 1 facilitating comparison across systems. Values close to 1 correspond to more resilient systems, following the definition given by Viejo (2009) and Grimm & Wissel (1997) as the speed at which an ecological system returns to a reference condition after a temporary disturbance.
- the return time to equilibrium (Fig. 2B) after a disturbance is $e = \frac{log(0.01)}{log(|p-q|)}$. This metric is related to the resilience index but gives the measure of time, as cells with a high resilience index will present a shorter return time. The return time can be site/system-specific, whereas the resilience index is a standardized metric allowing comparison with other systems.

Probabilities *p, 1-p* and *q* likely depend on the intertidal height range and shore and were derived from the drone image analyses by aggregating all cells from the overlapped orthomosaics at each specific intertidal height range from the West or East shore. We used the equations and the observed proportions of *Occupied, Lost*, and *Gained* cells to estimate the two parameters *p* and *q* for each shore and intertidal height range. One approach to achieve this is by utilizing an algorithm that minimizes the difference *f* between predicted and observed proportions of *Occupied* and *Gained* cells. We defined *f* as:

$$f = \frac{1}{3}\sqrt{\left(\frac{q}{1-p+q} - Occupied\right)^2 + \left(q\frac{1-p}{1-p+q} - Lost\right)^2 + \left(q\frac{1-p}{1-p+q} - Gained\right)^2}$$

where *Occupied* represents the observed proportion of occupied cells averaged over 2019 and 2020, *Gained* represents the observed proportion of gained cells relative to the empty cells in 2019, i.e. gain probability, and *Lost* represents the observed proportions of lost cells. We used the *optimal* function of the R package to find *(p,q)* that minimizes *f*.

For each shore and intertidal height range, we used the metrics defined above to analyze and compare the properties of mussel cells in these microhabitats. The predicted proportion of *Occupied* cells relative to the *Empty* cells would not change over time if the system is in equilibrium. Since observed values in 2019 and in 2020 were different, we assumed that some additional disturbance occurred between the two years and we estimated the time needed to reach equilibrium, denoted as the return time. Since the proportions of *Occupied* and *Empty* cells at equilibrium are asymptotic values, we defined the time to get as close as 1% of the equilibrium values with an initial proportion of *Occupied* cells equal to 0 (see Supplementary 2).

Results

Accuracy of the identified mussels' distribution dynamics

The accuracy of the image classification process was very good, with more than 79% of agreement between cells identified as mussel cells and the true mussel cells, as indicated by the Kappa index, across the two shores and dates studied (Table 1). The overall accuracy of the image classification was high, with 93% to 98% of evaluated cells correctly classified among the processed image datasets (Table 1).

Observed mussel's distribution dynamics

From the initially covered area in June 2019 (58.3 m^2), 80% (46.6 m^2) was lost, and 48% (27.9 m^2) was gained on the West shore, whereas in the East (280 m^2 in 2019), 55% (154.0 m^2) of the covered area was lost, and 14% (38.2 m^2) was gained (Table 2, Fig.3). The gained area was, thus, smaller than the lost area, resulting in a net decrease of the covered area of 32% and 41% on the West and East shores, respectively (Table 2, Fig. 3).

The probabilities of loss, persistence and gain varied principally between the West and East shores and among intertidal height positions, slope and orientation (Fig. 4). Between shores, the West presented higher loss probabilities and lower persistence probabilities than the East shore, mainly in the mid-intertidal area, whereas the gain probabilities were low on both shores and along the entire intertidal height gradient (Fig. 4). The loss probability and persistence probability varied from 0 to 1 in the West and East shore (Fig. 4). The gain probability varied between 0 and 0.22 and between 0 and 0.39 in the microhabitats of the West and East shore, respectively (Fig. 4). Along the intertidal height gradient, the loss and persistence probabilities presented a pattern with lower loss and higher persistence probability in the mid-intertidal height, mainly on the East shore, but no evident pattern was observed in the gain probability on both shores (Fig. 4). Regarding the microhabitat slope and orientation, there was no evident pattern either at specific intertidal positions or shore (Fig. 4).

Analyzing the proportion of variance explained by each of these factors also evidenced the higher importance of intertidal height over the slope and orientation of microhabitats on the probabilities of loss, persistence, and gain (Fig. 5, Table S1 in Supplementary 1). This highlighted that topographic features impact the two shores differently, with higher effects observed in the East compared to the West shore. The total variance not explained by either intertidal height, slope, and orientation (white area; Fig. 5) was higher in the West shore (76.9% to 80.1%) than in the East (36.1% to 66.6%), indicating an effect of the shore on the observed patterns of loss, persistence, and gain. A large part of the variance observed in the West shore would therefore be associated with another factor not related to the topographic features studied here. In the East shore, intertidal height dominates and explained 53.6% and 58.3% of the loss and persistence variation, respectively, while it explained only 9.1% and 13.6% on the West shore. Contrarily, the variance explained by slope and orientation was small and relatively similar between West and East shores, ranging from 0.5 to 1.2% and from 0.3 to 4.1% for slope and orientation, respectively.

Considering the dominating effect of intertidal height on mussel distribution dynamics, we explored how mussels' loss, persistence, and gain probabilities were distributed along both East and West intertidal heights. The distribution of their probabilities showed different patterns along the intertidal height (Fig. 6). On both shores, the persistence showed an unimodal distribution along the intertidal height, distributed on a wider range of values on the East shore and centered on 4.5 m above the LAT, relative to the West where values were observed over a lower range, between 4.3 m and 5.3 m, and centered on 4.7 m above the LAT. Gain probabilities showed a more similar unimodal pattern between shores, centered on 4.5 m

above the LAT (Fig. 6; note the different scales). The loss probability presented an inverse pattern relative to the persistence, with a bimodal distribution on both shores, with maxima observed at both margins, through the top and bottom intertidal heights (Fig. 6).

Properties of the mussel dynamics predicted by Markov model

Based on the major effect of the rocky shore and intertidal height on the probabilities of loss, persistence, and gain, we estimated model parameters along the intertidal height on each rocky shore. The comparison between observation and model predictions indicated that the model underestimates the occupancy of mussels in 2019 and overestimates the occupancy in 2020 (Fig. 7). This is due to the estimation procedure of model parameters, which assumes that the predicted occupancy ratios lie in between the values observed in 2019 and 2020. Predicted loss probabilities were very close to observations as opposed to the predicted gains probabilities, which were overestimated by the model (Fig. 7). This is again explained by the criterion used in the estimation procedure, which gives a larger weight to large values (e.g., Loss - see Methods).

The time to return to stable *Occupied* and *Empty* proportions after a disturbance varied between 2 and 8 years (Fig. 8A). The resilience index was above 0.5 for all combinations of shore and intertidal height, indicating a high capacity to return to equilibrium (Fig. 8B). Resilience is inversely (but not linearly) correlated to Return time (see Methods). Resilience was higher on the West than on the East shore, which corresponded with a slightly shorter return time shown by the simulations (Fig. 8B). For both shores, resilience was lower in the mid intertidal zone, around 4.6 m above the LAT. The persistence time and resilience index distribution along the intertidal height were opposite. Persistence time was higher on the East shore and varied along the intertidal height with maximum values of 3.7 years at intermediate intertidal height (Fig. 8C).

Discussion

Using drone images and a Markov chain model, we showed that the covered area by mussels (*Mytilus galloprovincialis*) on rocky shore habitats over a year was highly dynamic and spatially heterogeneous. The proportion of area with loss, gain, and persistence of mussels differed between the two rocky shores studied and among intertidal height ranges but they were quite similar among microhabitats of different slopes and orientations. Our results then support our first hypothesis about the persistence of covered areas determining the higher occupied proportion of the area at intermediate intertidal height and its decrease at the top and bottom edges. On the contrary, our second hypothesis about the effect of microhabitat slope and orientation on the dynamics of occupancy was not supported, since the variation related to these features represented less than 4% of the overall variation. The modeling approach showed a higher capacity of the population to recover from a disturbance at the top and bottom intertidal edges (maximum resilience index greater than 0.5 and return time lower than 3 years), as well as the potential of intermediate intertidal height areas to persist over 3.5 years in the absence of disturbance. In the following, we discuss the spatial heterogeneity of mussel dynamics and associated predicted long-term population properties (resilience and persistence time) and how they may relate to environmental factors or population traits. Finally, we discuss the value of combining observations and modeling in the study of population ecology.

Mussels occupancy and temporal dynamics

The mussel-covered areas in "Le Petit Minou" decreased substantially, between 50% and 80%, from June 2019 to June 2020 on both rocky shores and were only partially recovered. This highly dynamic character is not specific to the studied population and has also been described for mussels in different ecosystems. For example, monitoring of a wild population of *M. californianus* in the Northwest Pacific showed that natural disturbance in a rocky shore led to annual losses from 30% to 40% during the 1970-1978 period (Paine & Levin 1981). Other studies, based on experimental disturbance approaches and monitoring of small areas on rocky shores in Rhode Island, Northwest Atlantic, highlighted highly dynamic seasonal cover loss and recovery of mussels in the middle intertidal zone (0.5 to 1.0 m above mean lower low water). By monitoring fixed quadrats over a 3-yr period (2001-2003), Carrington et al. (2009) showed a cover loss of about 50% in the first year followed by stability and recovery or gain in the third year, a similar recovery time as our prediction for the East shore from "Le Petit Minou". Another quadrat showed about 20% of loss area in the first years, followed by a similar

recovery and a subsequent loss of ca. 40% which was not recovered in the second year, but increased in the third year reaching ca. 100% of loss, which was recovered to 70% coverage in only ca. 4 months. These results showed the high spatial variability and temporal dynamic in loss and recovery at a single intertidal range.

Our methodological approach, using remote-sensing imagery, provides extensive coverage of the mussel habitat and has enabled us to show that mussels' distribution dynamics varied principally along the intertidal height gradient on both shores, with between 8 to 58% of the variation related to it. This supports our first hypothesis that the persistence of mussel aggregations determines the higher occupancy at intermediate intertidal height. In other words, our results showed that the spatial distribution of disturbance, observed as lost areas, could determine the unimodal distribution of mussels along the intertidal gradient. This suggests that there is an optimum habitat for *M. galloprovincialis* when intertidal height is between 3.8 and 5 m above the LAT. Based on mussels' dynamics observation, Markov chain modeling showed that the pattern of persistence time was consistent with the observed persistence probabilities and, thus, higher at this optimum intertidal height. Mussels were predicted to reach a maximum persistence time of 3.7 years at intermediate intertidal height and about 1 year at the distribution edges. That estimation appears much lower than the maximum age of mussels individuals recorded in "Le Petit Minou", which was about 12 years old based on sclerochronology analyses (Barbosa et al. 2021). Such a mismatch could reflect the randomness of a few individuals reaching such an age of 12 years. The model simplifies the dynamics of mussels in a square area and assumes a complete change of state in such an area, whereas in reality, even in a disturbed area, some individuals can persist and create mussel aggregations of heterogeneous age as observed in-situ (e.g., Barbosa et al. 2021). In addition to the pattern of persistence time, our modeling approach showed an intertidal pattern of the resilience index and return time, which suggested that the population distribution is highly resilient mainly in the top and bottom edges of the intertidal range. It could sound contradictory since the areas with a lower resilience are the most occupied. However, mid-intertidal areas had a lower loss probability, which suggests that the ecological strategy is likely to increase their resilience in areas with higher disturbance. Higher resilience was also recorded at higher intertidal position, with higher environmental stress in macroalgal communities (Viejo 2009). The predicted return time at mid-intertidal height was in concordance with slow recovery in mussel coverage in wave-exposed areas in Patagonia, from 5 to 15% recovery after 3 years of experimental disturbance (Bertness et al. 2006). The trade-off between disturbance probability and resilience

426 could explain how the species can inhabit the upper and lower intertidal areas, where, without
427 a high recovery capacity, mussels would disappear over time.
428 Contrary to expected, the spatial distribution of loss and gain probability (i.e., the
429 dynamics of mussels' distribution) recorded between 2019 and 2020 was only marginally
430 related to microhabitat slope and orientation. This result may seem contradictory to
431 observations made by Harley et al. (2008) who found higher mortality in microhabitats oriented
432 to the south during high temperature periods. However, our one-year period dynamics balance
433 must limit our ability to identify the effect of microhabitat features at specific seasons, since
434 disturbance patterns must vary among seasons. Furthermore, our results also contradict
435 observations made by Barbosa et al. (2022), who showed a link between the distribution of
436 mussels on the East shore of "Le Petit Minou" in 2019 and microhabitats' features. The
437 occupancy pattern recorded on the East shore should thus result from a different process than
438 disturbance either between 2019 and 2020 or even before 2019. Another potential explanation
439 could be that a cumulative effect of longer-term processes would produce the observed
440 occupancy pattern linked to orientation and slope, and short-term disturbances would be mainly
441 linked to the intertidal height profile and the effect of shore (i.e., mesoscale).
442
443 **Potential factors driving the distribution dynamics**
444 Our observations of a net decrease in the total occupied area indicated that the gained
445 area was not enough to compensate for the loss of individuals in a period of a year. The system
446 was, therefore, not at equilibrium, i.e., it does not have a constant proportion of *Occupied* vs.
447 *Empty* area over time, which calls for an explanation based on one or more sources of
448 disturbance. The low gain area observed in the present study indicated slow recolonization
449 during the 2019-2020 period. Recolonization of lost areas occurs generally by the growth of
450 individuals still in place and movement of individuals from the perimeter of the lost areas, also
451 called clearings or gaps, while recruitment in such bare areas is almost insignificant (Paine &
452 Levin 1981, Littorin & Gilek 1999). The growth rate of mussels on both shores is generally
453 low, with estimates of less than 1 cm growth over a year (Barbosa et al. 2021). This could
454 explain the observed low gain area in only one year. Differently, in subtidal habitats, mussels'
455 growth rate seems to determine the differences in coverage and biomass among depths (Gilek
456 et al. 2001). This must be related to the lower effect of waves and the independence from tides
457 effect on the feeding time on subtidal areas, whereas we showed that in intertidal rocky shores,
458 the intertidal height position, which determines the immersion time, was the main factor related
459 to the dynamic of mussels.

Mussel bed disturbances are mainly known to be related to wave action and temperature (Harger & Landenberger 1971, Paine & Levin 1981, Denny 1987, Harley & Helmuth 2003, Guichard et al. 2003, Harley 2008, Carrington et al. 2009, Seuront et al. 2019). Combined conditions of high-temperature stress and wave action cause extreme mortality by dislodgement in summer, when mussels' attachment is generally weaker (Carrington 2002, Carrington et al. 2008, 2009). The high loss observed in our study area could result from this type of extreme event. Indeed, an event combining high spring and summer temperatures compared to long-term records and a period of high waves occurred in early August (Figure S1 in Supplementary 1). The occurrence and intensity of marine heatwaves have been increasing over the last decade as a result of global warming in the Bay of Biscay, English Channel and Bay of Brest (Simon et al. 2023). Consequently, disturbances of mussel distribution related to marine heatwaves are likely occurring at a larger spatial scale and a higher frequency.

Sand dynamics can also affect mussel distribution, mainly at the lower intertidal level (Zardi et al. 2008, Bagur et al. 2022). Sand dynamics increases mussels' mortality and determines mussels' lower limit of distribution in other areas (Zardi et al. 2008, Bagur et al. 2022). Sand intertidal level in the studied site was observed to change by about 1 m in height during the winter of 2019 (Fourer et al. 2023). These movements of the sand and changes to the overall topography of the site may have caused additional disturbance, helping to explain the low rate of gain observed. Sea star predators, which determine lower limits in the Northwest Pacific, are almost absent in our study area (Tsuchiya and Retiere, 1988). This would not play a main role in the limit of mussel range, as also observed in Patagonia (Bertness et al. 2006), which supports the possibility of sand dynamics limiting mussels' lower distribution.

Spatial variability in disturbance sources, combined with differences in biological features of mussel aggregations between shores, could explain differences in mussel cover dynamics between the East and West shores. Mussel aggregations in the West appear to be less stable, presenting a higher probability of loss and consequently lower persistence than those in the East. Differences in wave exposure and sun exposure are expected between the East and West shores, given their distinct orientations. These differences in exposure to sun and waves could result in differences in the average temperatures experienced by individual mussels (Helmuth & Denny 2003, Gilman et al. 2006, Seabra et al. 2011). Potentially higher sun exposure and temperature could intensify the combined effect of waves and thermal stress. Furthermore, patterns of mussel occupancy were related to mesoscale orientation differences between shores (Barbosa et al. 2022). Population features, such as density and crowding

structure, could also influence the effect of disturbance. Disturbance would spread through direct neighbors, and the formation of hummocks tends to decrease the attached surface when density increases (Tanaka & Magalhães 2002, Guichard et al. 2003, Gutiérrez et al. 2015). Similarly, the density of aggregations and substrate type can influence the recolonization, i.e., gain, of mussels (Bertolini et al. 2018). The density of mussels is higher in the West than in the East shore, with a higher recruitment and lower growth rate (Barbosa et al. 2021). All these features could explain the higher resilience estimated for the West compared to the East shore.

The major heterogeneity in mussel dynamics along the intertidal height, compared to the microhabitat slope and orientation, could reflect the marked tidal dynamics throughout the year compared to horizontal spatial change conditions. A tidal cycle would be relatively similar throughout the entire year (e.g., the lower intertidal remains always submerged for a longer period), whereas no particular pattern favoring specific orientation and slope emerges due to the high seasonality of temperature and waves exposure at a small scale (Littorin & Gilek 1999, Gilek et al. 2001). For instance, Helmuth & Denny (2003) highlighted the difficulty of classifying microhabitats based on the hydrodynamic forces experienced by individuals living there, due to the high temporal and spatial heterogeneity in wave microscale forces (see also Burel et al. 2019, Focht & Shima 2020, Gaylord 1999).

Other processes such as the spreading of disturbance and density-linked stochasticity, as well as some limitations of our methods could create noise that impacts the identification of a microhabitat effect on the probability of loss. In reality, the spreading of the disturbance among neighbors could cause a larger loss than the one produced by the actual disturbance (Denny 1987, Guichard et al. 2003). Furthermore, density-linked stochasticity has been predicted to play an important role in the long-term dynamic of mussels (Wootton & Forester 2013). Between the limitations of our methods, the resolution of microhabitat features (slope and orientation; 20 x 20 cm resolution), could affect the analysis. Then, we do not discard the potential relationship between the slope and orientation on the probability of an initial loss of individuals, which could then expand to all microhabitat areas where the aggregation of mussels is connected.

Interest and limits of the modeling approach

Markov chain theory proved to be useful in describing temporal dynamics in population ecology, e.g., long term persistence (Pandolfo et al. 2017), succession between species or functional groups (Wootton 2001, Wootton 2004, Hill et al. 2004, Tsujino et al. 2010) or species extinction (Hill et al. 2002). The matrix of transition probabilities between states help comparing sites, assessing patterns of local biodiversity and evaluating changes over time.

Going a step further, Wootton (2004) computed system resilience and assessed the contribution of each functional group using a Markov model with a dozen of states based on successions between functional groups. Pandolfo et al. (2017) derived transition probabilities over 26 years and computed persistence of mussel assemblages. In our study, we derived resilience, return time and persistence time of mussel covered areas from the transition matrix between 2 states. Though we only gave the equations for this simple system, these properties could be easily computed for systems with more than 2 states.

Estimation of model parameters is usually based on monitoring quadrats (Tsujino et al., 2010) or experiments (Guichard et al. 2003, Wootton 2004). One important difference with our study is that we had a full coverage of the studied area, which reinforces the accuracy of the estimation of transition probabilities. On the other hand, we made observations at only two different dates and results showed an important change in the areas covered by mussels. This change reflects the stochasticity of the occupation process and yields uncertainty in the estimation of model parameters. We therefore made the assumption that the predicted occupancy lies between the values derived from the observations made at 2 different dates. Additional observations would likely yield the same patterns linked to the effects of intertidal height and shore orientations, even though the values of predicted persistence time, resilience and return time would differ from our actual results. Monitoring mussel distribution over a longer period of time would therefore help estimating model parameters more precisely.

We explained that the gradient of environmental drivers would result in different transitions between states. One perspective is to move towards more explicit formulations of mechanisms which account for the variability of species distributions over space and time. Such a mathematical formulation would allow assessing local interactions and pattern formations. For instance, Guichard et al. (2003) used a spatially explicit Markov Chain model to predict patterns emerging from local interactions. In their approach, the recovery probability of an empty cell mimics the lateral movement of adult mussels into bare space and depends on the proportion of occupied nearest neighbors in a regular spatial grid. They explored the response of spatial patterns (e.g. edges between occupied and empty cells) to environmental conditions through the sensitivity of model properties to parameter setting. As a consequence, they suggest that Markov models help inform on environmental drivers of mussel bed spatial patterns at local and large scales. High-resolution imaging could therefore be combined to a mechanistic model of spatial interactions at a small scale to quantify more precisely how local disturbances, movement and settlement of new individuals explain the differences in temporal dynamics among intertidal heights that we predicted.

Conclusions and perspectives

Our analyses allowed for an evaluation of mussel distribution dynamics over one-year, with changes observed at a spatial resolution of one centimeter along two entire rocky shores. Our results outline the role of intertidal height on the temporal and spatial dynamics of mussel distribution, the occurrence of major disturbance, and the probability of long-term persistence. This work highlights the power of image analyses in the study of spatial ecological processes related to disturbances, which has predominantly been explored through experiments conducted in limited, specific areas (generally small square areas). A monitoring strategy incorporating more frequent surveys, alongside ongoing temperature monitoring projects (e.g., Seabra et al. 2015, Seuront et al. 2019) would enable the assessment of seasonality in population dynamics, including responses to events such as storms, and the identification of the main drivers involved. The use of drone images in conjunction with modeling approaches would be particularly apt for long-term monitoring, shedding light on the long-term persistence of populations facing changes in the frequency and intensity of marine heatwaves (Simon et al. 2023).

Funding

This study and RVB benefited from the financial support of the Region Bretagne and Université de Bretagne Occidentale (UBO). Scientific committee of IUEM funded student's training related to the project.

References

Arribas LP, Donnarumma L, Palomo MG, Scrosati RA (2014) Intertidal mussels as ecosystem engineers: their associated invertebrate biodiversity under contrasting wave exposures. Mar Biodivers 44:203–211.

Bagur M, Gutiérrez JL, González JA, Arribas LP, Palomo MG (2022) Physical rather than biotic factors set the lower limit of mussel beds in a horizontal rocky intertidal platform. J Exp Mar Biol Ecol 548:151680.

Barbosa RV, Bacher C, Jean F, Thomas Y (2021) Individual traits and population parameters of a rocky-shore mussel population.

Barbosa RV, Jaud M, Bacher C, Kerjean Y, Jean F, Ammann J, Thomas Y (2022) High-Resolution Drone Images Show That the Distribution of Mussels Depends on Microhabitat Features of Intertidal Rocky Shores. Remote Sens 14:5441.

Bagur M, Gutiérrez JL, González JA, Arribas LP, Palomo MG (2022) Physical rather than biotic factors set the lower limit of mussel beds in a horizontal rocky intertidal platform. Journal of Experimental Marine Biology and Ecology 548:151680.

598 Bertness MD, Crain CM, Silliman BR, Bazterrica MC, Reyna MV, Hildago F, Farina JK
599 (2006) The Community Structure of Western Atlantic Patagonian Rocky Shores.
600 Ecological Monographs 76:439–460.
601 Bierne N, Borsa P, Daguin C, Jollivet D, Viard F, Bonhomme F, David P (2003) Introgression
602 patterns in the mosaic hybrid zone between *Mytilus edulis* and *M. galloprovincialis*.
603 Molecular Ecology 12:447–461.
604 Bertolini C, Montgomery WI, O'Connor NE (2018) Habitat with small inter-structural spaces
605 promotes mussel survival and reef generation. Mar Biol 165:163.
606 Borthagaray AI, Carranza A (2007) Mussels as ecosystem engineers: Their contribution to
607 species richness in a rocky littoral community. Acta Oecologica 31:243–250.
608 Burel T, Schaal G, Grall J, Le Duff M, Chapalain G, Schmitt B, Gemin M, Boucher O, Ar
609 Gall E (2019) Small-scale effects of hydrodynamics on the structure of intertidal
610 macroalgal communities: A novel approach. Estuar Coast Shelf Sci 226:106290.
611 Carrington E (2002) Seasonal variation in the attachment strength of blue mussels: Causes
612 and consequences. Limnol Oceanogr 47:1723–1733.
613 Carrington E, Moeser GM, Dimond J, Mello JJ, Boller ML (2009) Seasonal disturbance to
614 mussel beds: Field test of a mechanistic model predicting wave dislodgment. Limnol
615 Oceanogr 54:978–986.
616 Carrington E, Moeser GM, Thompson SB, Coutts LC, Craig CA (2008) Mussel attachment
617 on rocky shores: the effect of flow on byssus production. Integr Comp Biol 48:801–
618 807.
619 Choi F, Gouhier T, Lima F, Rilov G, Seabra R, Helmuth B (2019) Mapping physiology:
620 biophysical mechanisms define scales of climate change impacts. Conserv Physiol
621 7:coz028.
622 Cohen J (1960) A Coefficient of Agreement for Nominal Scales. Educ Psychol Meas 20:37–
623 46.
624 Congalton RG (1991) A review of assessing the accuracy of classifications of remotely
625 sensed data. Remote Sens Environ 37:35–46.
626 Curd A, Chevalier M, Vasquez M, Boyé A, Firth LB, Marzloff MP, Bricheno LM, Burrows
627 MT, Bush LE, Cordier C, Davies AJ, Green JAM, Hawkins SJ, Lima FP, Meneghesso
628 C, Mieszkowska N, Seabra R, Dubois SF (2023) Applying landscape metrics to
629 species distribution model predictions to characterize internal range structure and
630 associated changes. Glob Change Biol 29:631–647.
631 Dayton PK (1971) Competition, Disturbance, and Community Organization: The Provision
632 and Subsequent Utilization of Space in a Rocky Intertidal Community. Ecol Monogr
633 41:351–389.
634 Denny MW (1987) Lift as a mechanism of patch initiation in mussel beds. J Exp Mar Biol
635 Ecol 113:231–245.
636 Feurer D, Vinatier F (2018) Joining multi-epoch archival aerial images in a single SfM block
637 allows 3-D change detection with almost exclusively image information. ISPRS J
638 Photogramm Remote Sens 146:495–506.
639 Focht RC, Shima JS (2020) Acceleration loggers reveal fine-scale heterogeneity in wave
640 exposure along an open coast. Estuar Coast Shelf Sci 233:106507.
641 Garza C (2019) Landscape Ecology in the Rocky Intertidal: Opportunities for Advancing
642 Discovery and Innovation in Intertidal Research. Curr Landscape Ecol Rep 4:83–90.
643 Gaylord B (1999) Detailing agents of physical disturbance: wave-induced velocities and
644 accelerations on a rocky shore. J Exp Mar Biol Ecol 239:85–124.
645 Gilek M, Littorin B, Saetre P (2001) Spatial patterns of abundance and growth of *Mytilus*
646 *edulis* on boulders in the Northern Baltic Sea proper. Hydrobiologia 452:59–68.
647 Gilman SE, Wethey DS, Helmuth B (2006) Variation in the sensitivity of organismal body

temperature to climate change over local and geographic scales. Proc Natl Acad Sci 103:9560–9565.
Gomes I, Peteiro L, Bueno-Pardo J, Albuquerque R, Pérez-Jorge S, Oliveira ER, Alves FL, Queiroga H (2018) What's a picture really worth? On the use of drone aerial imagery to estimate intertidal rocky shore mussel demographic parameters. Estuar Coast Shelf Sci 213:185–198.
Grimm V, Wissel C (1997) Babel, or the ecological stability discussions: an inventory and analysis of terminology and a guide for avoiding confusion. Oecologia 109:323–334.
Guichard F, Bourget E, Agnard J-P (2000) High-resolution remote sensing of intertidal ecosystems: A low-cost technique to link scale-dependent patterns and processes. Limnol Oceanogr 45:328–338.
Guichard F, Bourget E, Robert J (2001) Scaling the influence of topographic heterogeneity on intertidal benthic communities: alternate trajectories mediated by hydrodynamics and shading. Mar Ecol Prog Ser 217:27–41.
Guichard F, Halpin PM, Allison GW, Lubchenco J, Menge BA (2003) Mussel Disturbance Dynamics: Signatures of Oceanographic Forcing from Local Interactions. Am Nat 161:889–904.
Gutiérrez J, Palomo M, Bagur M, Arribas L, Soria S (2015) Wave action limits crowding in an intertidal mussel. Mar Ecol Prog Ser 518:153–163.
Harger JRE, Landenberger DE (1971) The effect of storms as a density dependent mortality factor on population of sea mussels. Veliger 14:195–201.
Harley C (2008) Tidal dynamics, topographic orientation, and temperature-mediated mass mortalities on rocky shores. Mar Ecol Prog Ser 371:37–46.
Harley CDG, Helmuth BST (2003) Local- and regional-scale effects of wave exposure, thermal stress, and absolute versus effective shore level on patterns of intertidal zonation. Limnol Oceanogr 48:1498–1508.
Helmuth B (2002) How do we Measure the Environment? Linking Intertidal Thermal Physiology and Ecology Through Biophysics1. Integrative and Comparative Biology 42:837–845.
Helmuth B, Choi F, Matzelle A, Torossian JL, Morello SL, Mislan K a. S, Yamane L, Strickland D, Szathmary PL, Gilman SE, Tockstein A, Hilbish TJ, Burrows MT, Power AM, Gosling E, Mieszkowska N, Harley CDG, Nishizaki M, Carrington E, Menge B, Petes L, Foley MM, Johnson A, Poole M, Noble MM, Richmond EL, Robart M, Robinson J, Sapp J, Sones J, Broitman BR, Denny MW, Mach KJ, Miller LP, O'Donnell M, Ross P, Hofmann GE, Zippay M, Blanchette C, Macfarlan JA, Carpizo-Ituarte E, Ruttenberg B, Peña Mejía CE, McQuaid CD, Lathlean J, Monaco CJ, Nicastro KR, Zardi G (2016) Long-term, high frequency in situ measurements of intertidal mussel bed temperatures using biomimetic sensors. Sci Data 3:160087.Helmuth B, Denny MW (2003) Predicting wave exposure in the rocky intertidal zone: Do bigger waves always lead to larger forces? Limnol Oceanogr 48:1338–1345.
Helmuth B, Yamane L, Lalwani S, Matzelle A, Tockstein A, Gao N (2011) Hidden signals of climate change in intertidal ecosystems: What (not) to expect when you are expecting. J Exp Mar Biol Ecol 400:191–199.
Hill MF, Witman JD, Caswell H (2004) Markov Chain Analysis of Succession in a Rocky Subtidal Community. The American Naturalist 164:E46–E61.
Hill MF, Witman JD, Caswell H (2002) Spatio-temporal variation in Markov chain models of subtidal community succession. Ecology Letters 5:665–675.
Hunt H, Scheibling R (2001) Predicting wave dislodgment of mussels: variation in attachment strength with body size, habitat, and season. Mar Ecol Prog Ser 213:157–

698 164.
699 Kruskal WH, Wallis WA (1952) Use of Ranks in One-Criterion Variance Analysis. 47:583–
700 621.
701 Lane DM Online Statistics Education: A Multimedia Course of Study
702 (http://onlinestatbook.com/). Project Leader: David M. Lane, Rice University
703 Littorin B, Gilek M (1999) A photographic study of the recolonization of cleared patches in a
704 dense population of *Mytilus edulis* in the northern Baltic proper. Hydrobiologia
705 393:211–219.
706 Meager J, Schlacher T, Green M (2011) Topographic complexity and landscape -temperature
707 patterns create a dynamic habitat structure on a rocky intertidal shore. Mar Ecol Prog
708 Ser 428:1–12.
709 Paine RT (1974) Intertidal community structure. Oecologia 15:93–120.
710 Paine RT, Levin SA (1981) Intertidal Landscapes: Disturbance and the Dynamics of Pattern.
711 Ecol Monogr 51:145–178.
712 Pandolfo TJ, Kwak TJ, Cope WG, Heise RJ, Nichols RB, Pacifici K (2017) Declining
713 Occurrence and Low Colonization Probability in Freshwater Mussel Assemblages: A
714 Dynamic Occurrence Modeling Approach. Freshwater Mollusk Biology and
715 Conservation 20:13–19.
716 Poloczanska ES, Brown CJ, Sydeman WJ, Kiessling W, Schoeman DS, Moore PJ, Brander
717 K, Bruno JF, Buckley LB, Burrows MT, Duarte CM, Halpern BS, Holding J, Kappel
718 CV, O'Connor MI, Pandolfi JM, Parmesan C, Schwing F, Thompson SA, Richardson
719 AJ (2013) Global imprint of climate change on marine life. Nat Clim Change 3:919–
720 925.
721 Scrosati RA, Arribas LP, Donnarumma L (2021) The Hidden Biodiversity of Intertidal
722 Mussel Beds under contrasting Wave Exposures. Bull Ecol Soc Am 102:e01811.
723 Seabra R, Wethey DS, Santos AM, Lima FP (2011) Side matters: Microhabitat influence on
724 intertidal heat stress over a large geographical scale. J Exp Mar Biol Ecol 400:200–
725 208.
726 Seuront L, Nicastro KR, Zardi GI, Goberville E (2019) Decreased thermal tolerance under
727 recurrent heat stress conditions explains summer mass mortality of the blue mussel
728 *Mytilus edulis*. Sci Rep 9:17498.
729 Silliman BR, Bertness MD, Altieri AH, Griffin JN, Bazterrica MC, Hidalgo FJ, Crain CM,
730 Reyna MV (2011) Whole-Community Facilitation Regulates Biodiversity on
731 Patagonian Rocky Shores. PLOS ONE 6:e24502.
732 Simon A, Arbiol C, Nielsen EE, Couteau J, Sussarellu R, Burgeot T, Bernard I, Coolen JWP,
733 Lamy J-B, Robert S, Skazina M, Strelkov P, Queiroga H, Cancio I, Welch JJ, Viard F,
734 Bierne N (2020) Replicated anthropogenic hybridisations reveal parallel patterns of
735 admixture in marine mussels. Evolutionary Applications 13:575–599.
736 Simon A, Poppeschi C, Plecha S, Charria G, Russo A (2023) Coastal and regional marine
737 heatwaves and cold spells in the northeastern Atlantic. Ocean Sci 19:1339–1355.
738 Tanaka MO, Magalhães CA (2002) Edge effects and succession dynamics in Brachidontes
739 mussel beds. Mar Ecol Prog Ser 237:151–158.
740
741 Thomas Y, Razafimahefa NR, Ménesguen A, Bacher C (2020) Multi-scale interaction
742 processes modulate the population response of a benthic species to global warming.
743 Ecol Model 436:109295.
744 Tsujino M, Hori M, Okuda T, Nakaoka M, Yamamoto T, Noda T (2010) Distance decay of
745 community dynamics in rocky intertidal sessile assemblages evaluated by transition
746 matrix models. Population Ecology 52:171–180.
747 Tsuchiya M, Retiere C (1988) Zonation of Intertidal Organisms and Community Structure of

748 Small Animals Associated with Patches of the Mussel *Mytilus edulis* L. along the
749 Rocky Coast of Dinard, Brittany, France. Bull Coll Sci, Univ Ryukyus 54:47–81.
750 Viejo RM (2009) Resilience in intertidal rocky shore assemblages across the stress gradient
751 created by emersion times. Mar Ecol Prog Ser 390:55–65.
752 Wootton JT (2001) Prediction in Complex Communities: Analysis of Empirically Derived
753 Markov Models. Ecology 82:580–598.
754 Wootton J (2004) Markov chain models predict the consequences of experimental extinctions.
755 Ecol Lett 7:653–660.
756 Wootton JT, Forester JD (2013) Complex Population Dynamics in Mussels Arising from
757 Density-Linked Stochasticity. PLOS ONE 8:e75700.
758 Zardi GI, Nicastro KR, McQuaid CD, Erlandsson J (2008) Sand and wave induced mortality
759 in invasive (*Mytilus galloprovincialis*) and indigenous (*Perna perna*) mussels. Mar
760 Biol 153:853–858.

761 **Table 1** Overall accuracy and Kappa index indicating the performance of the supervised
762 classification results performed for each shore and date.

Rocky shore	Dataset	Overall accuracy (%)	Kappa index
West	June 2019	0.98	0.93
	June 2020	0.93	0.79
East	June 2019	0.93	0.80
	June 2020	0.94	0.82

763

764 **Table 2** Summary of the dynamics of distribution in the West and East shores in "Le Petit
765 Minou". Percentages are calculated with respect to the total initial area of the corresponding
766 shore (2019; 100%).

Shore	Occupied Initial area, 2019 (m^2)	Occupied Final area, 2020 (m^2)	Net area difference m^2 (%)	Loss surface m^2 (%)	Persistence surface m^2 (%)	Gain surface m^2 (%)
West	58.3	39.5	-18.7 (32.2%)	46.6 (80%)	11.7 (20%)	27.9 (48%)
East	280.0	164.0	-116.0 (41.3%)	154.0 (55%)	126.0 (45%)	38.2 (14%)

767

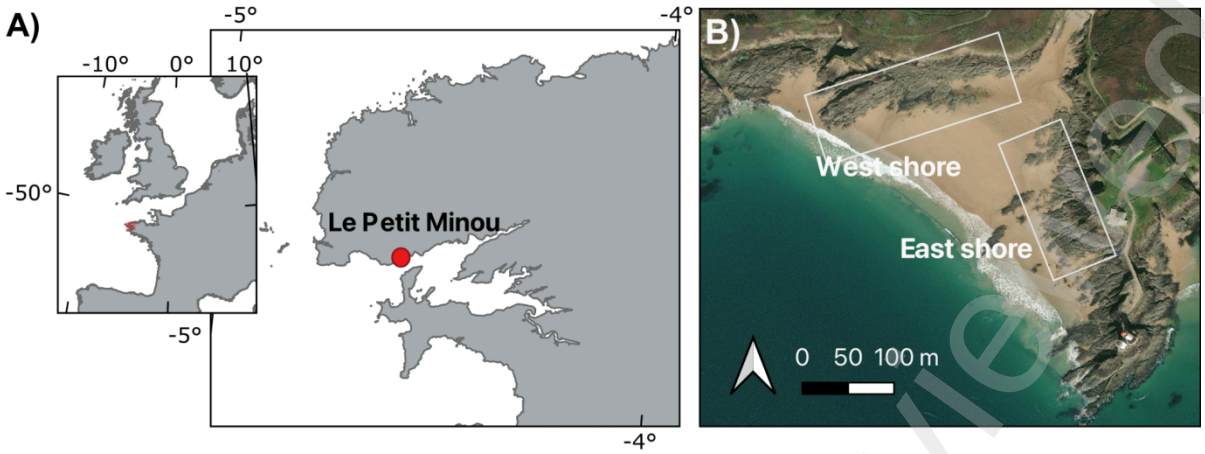

768

769 **Figure 1.** A) Study site location, "Le Petit Minou", France, and B) the West and East rocky
770 shore areas surveyed by the drone in "Le Petit Minou".

771

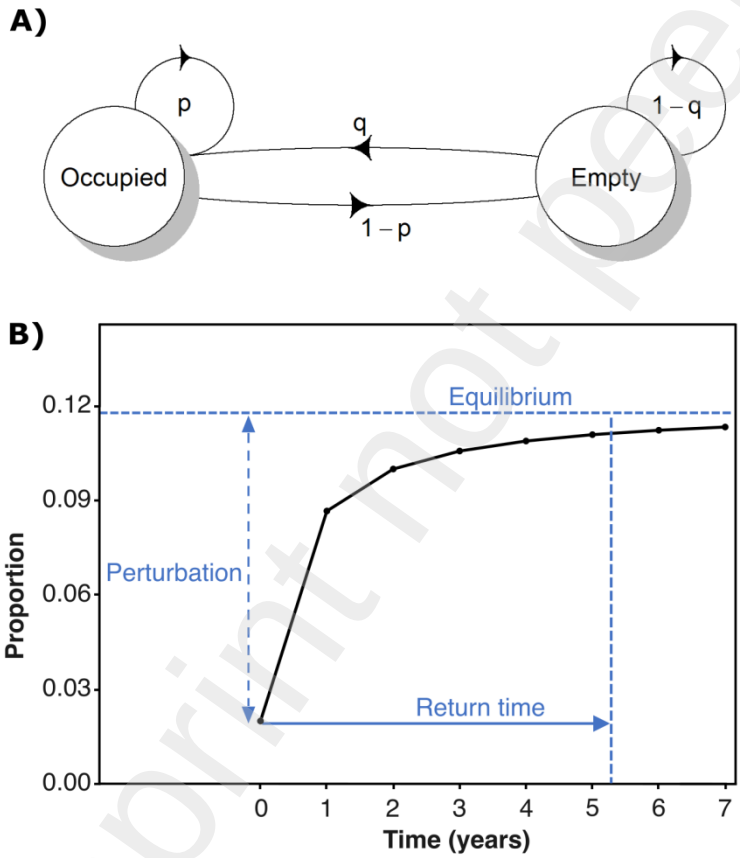

772

773 **Figure 2**. A) States and transition probabilities of cells for a specific intertidal height range
774 and shore. B) Temporal dynamics of a theoretical proportion of *Occupied* cells.

775

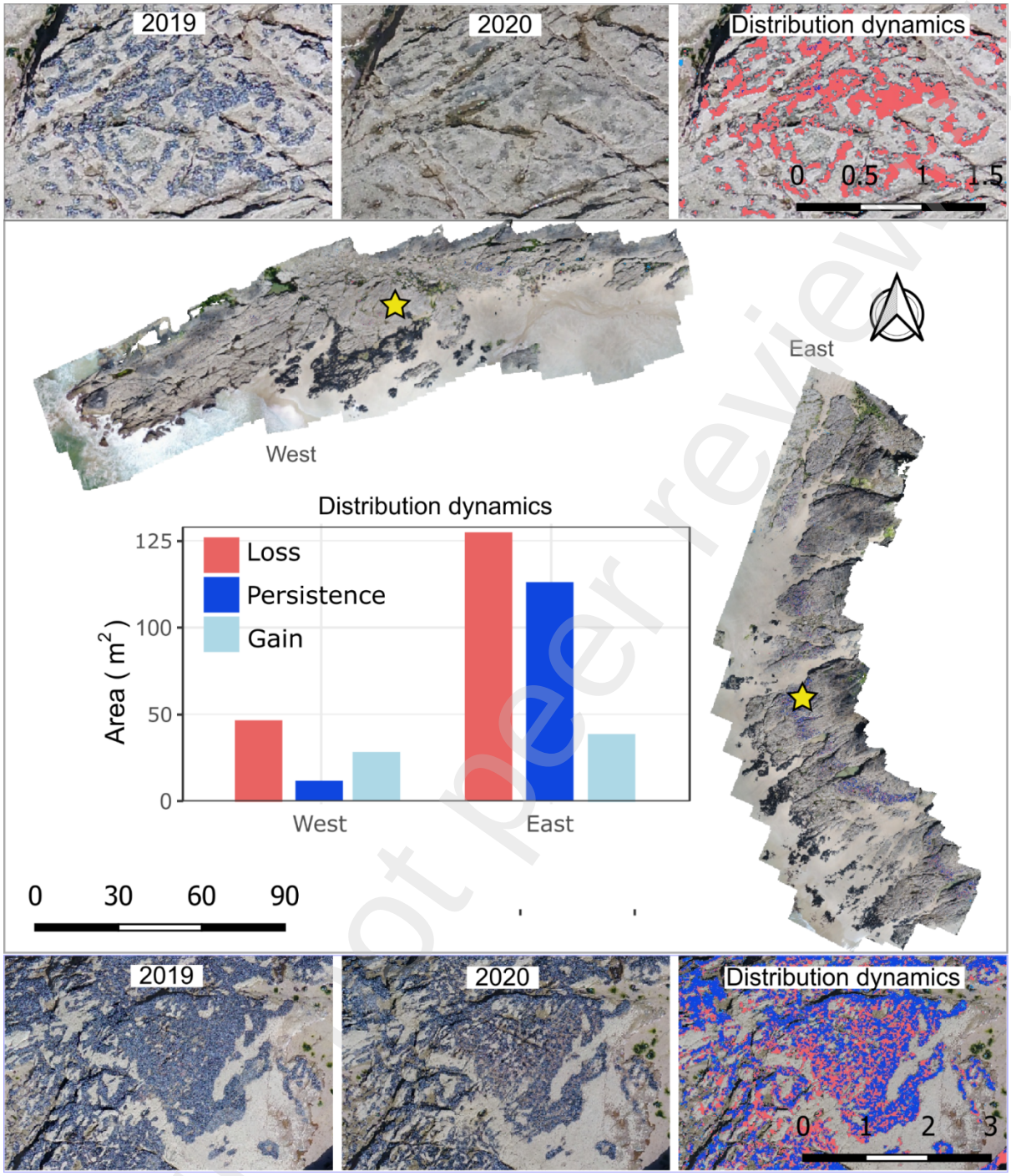

776

777 **Figure 3** Mussel coverage distribution dynamics between June 2019 and June 2020 in the West
778 and East rocky shore in "Le Petit Minou", France. Inset images from the West (top panels) and
779 East shore (bottom panels) show mussel occupancy in 2019 and 2020, along with the resultant
780 dynamics. Areas where individuals were present in 2019 but absent in 2020 (loss), areas
781 without mussels in 2019 but with mussel presence in 2020 (gain), and areas where mussels
782 were present in both 2019 and 2020 (persistence) are indicated. Yellow stars indicate the
783 location of inserted images; scale bars are in meters.

784

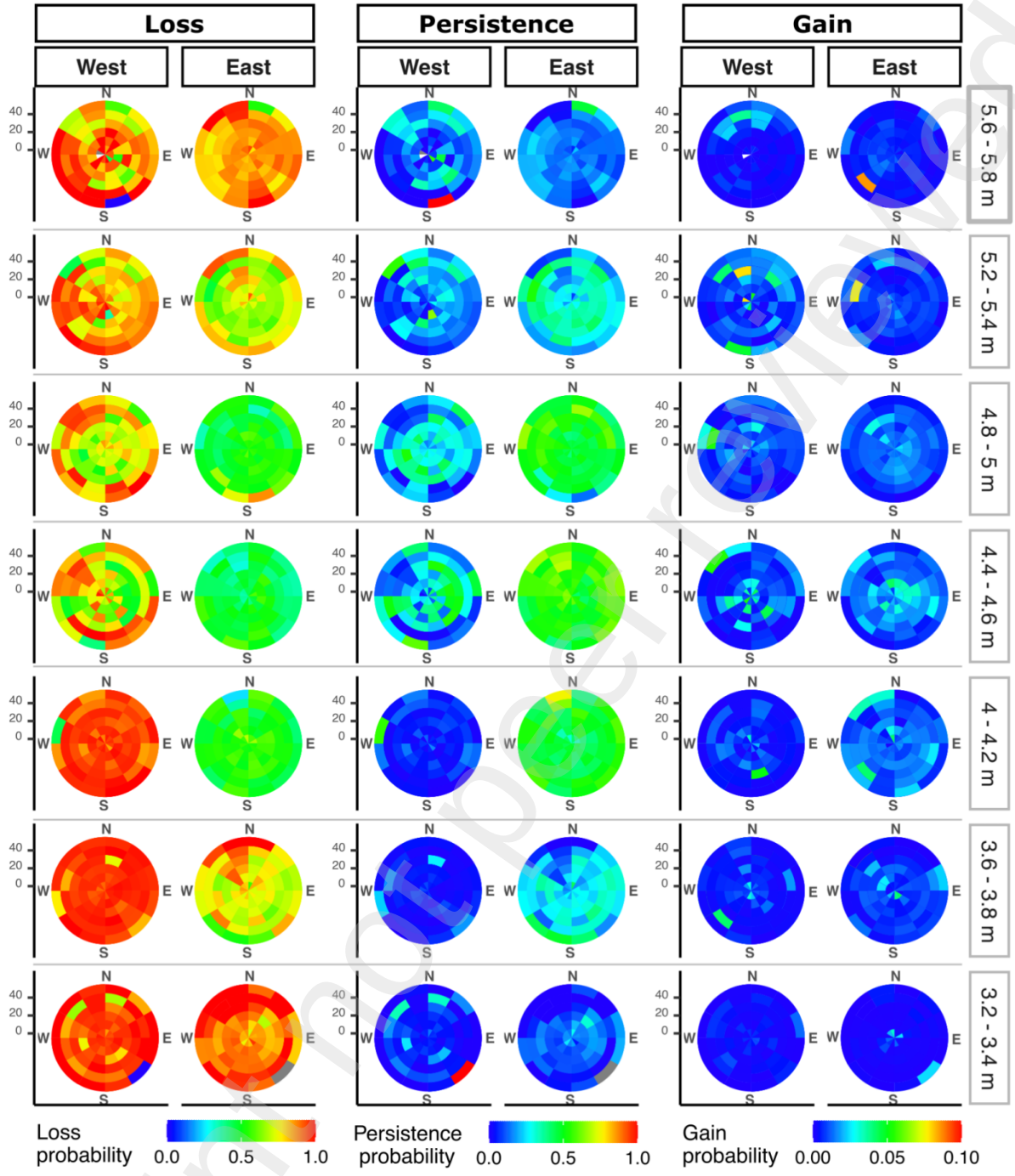

Figure 4. The probability of loss, persistence, and gain area for all microhabitats with different slopes (increasing from the center to the border), orientation (cardinal orientations indicated with letters; N: North, E: East, S: South, and W: West), and intertidal height (increasing from bottom to the top panels). Loss probability is the ratio of occupied cells in 2019 that become empty in 2020; Persistence probability is the ratio of occupied cells in 2019 that continue to be occupied in 2020; and Gain probability is the ratio of empty cells in 2019 that become occupied in 2020. Probabilities were averaged at each microhabitat type.

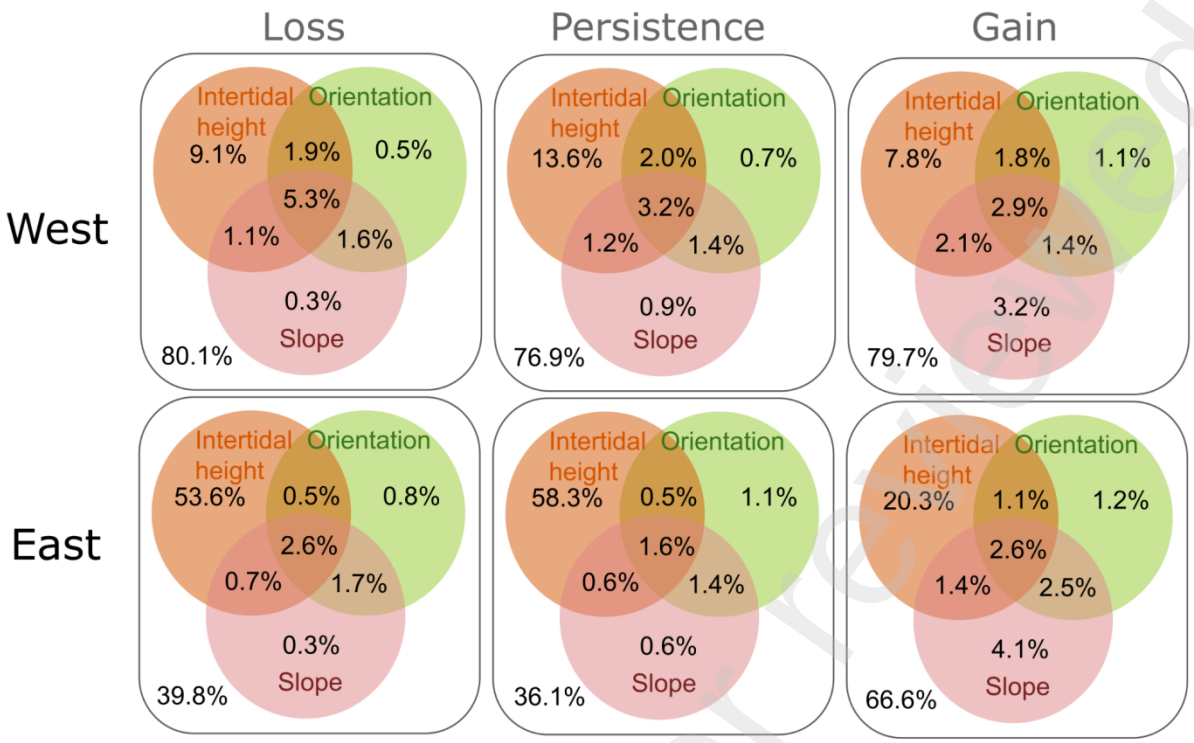

794

795 **Figure 5.** Venn diagrams with the percentage of variance (based on the sum of squares, Table
796 S1 in Supplementary 1), that was related to each of the three topographic features evaluated
797 (circles) and the interactions among them (overlapped areas). The percentage of variance not
798 explained by the topographic features is indicated with the white background area.

799

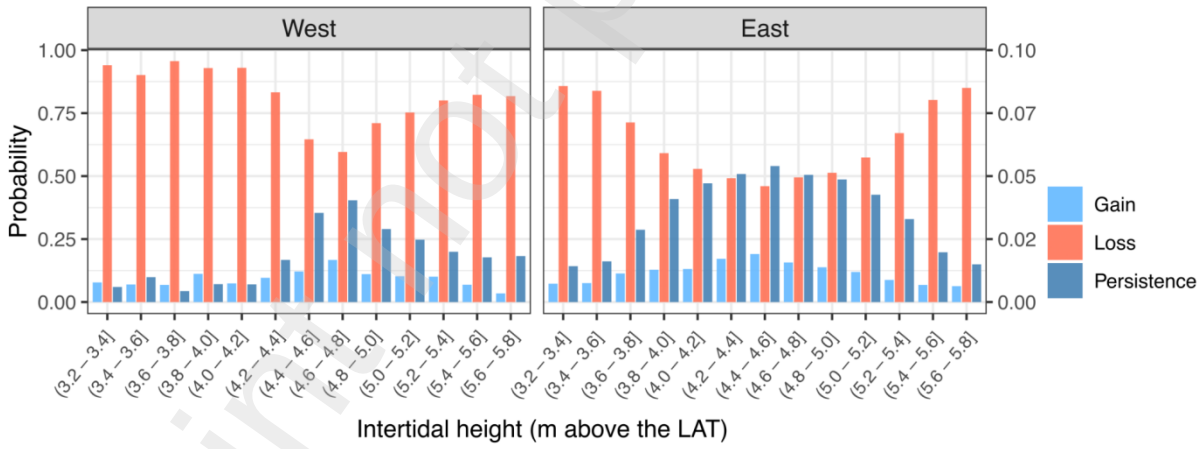

800

801 **Figure 6.** Relative distribution dynamics are represented as the probability of loss, persistence,
802 and gain at specific intertidal height range on the West and East shore. Loss probability is the
803 ratio of occupied cells in 2019 that become empty in 2020; Persistence probability is the ratio
804 of occupied cells in 2019 that continue to be occupied in 2020; and, Gain probability is the
805 ratio of empty cells in 2019 that become occupied in 2020. Probabilities were averaged at each
806 intertidal height range. The left axis represents Loss and Persistence probabilities, whereas the
807 right axis represents Gain probability.

808

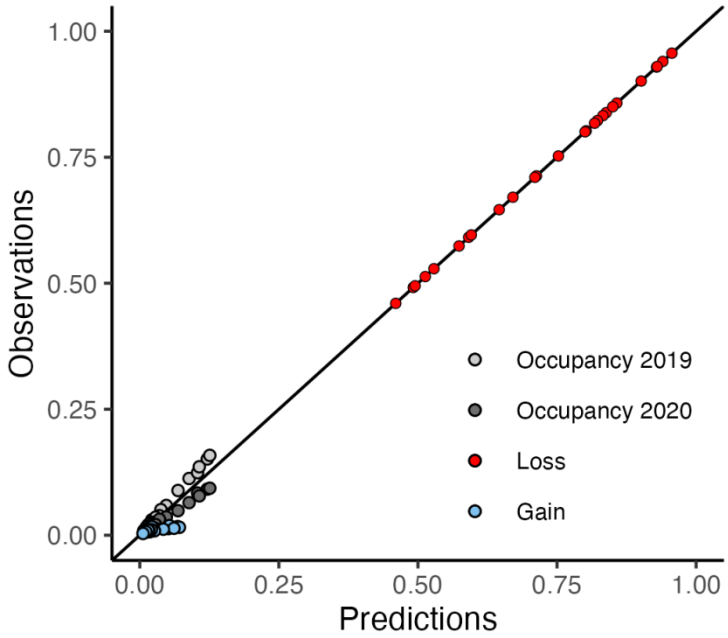

Figure 7. Comparison between observations and model predictions of gain probability, loss probability, and the proportion occupied in 2019 and 2020. Dots correspond to the intertidal heights in the two shores. The line represents the bisector and corresponds to perfect agreement between observations and predictions.

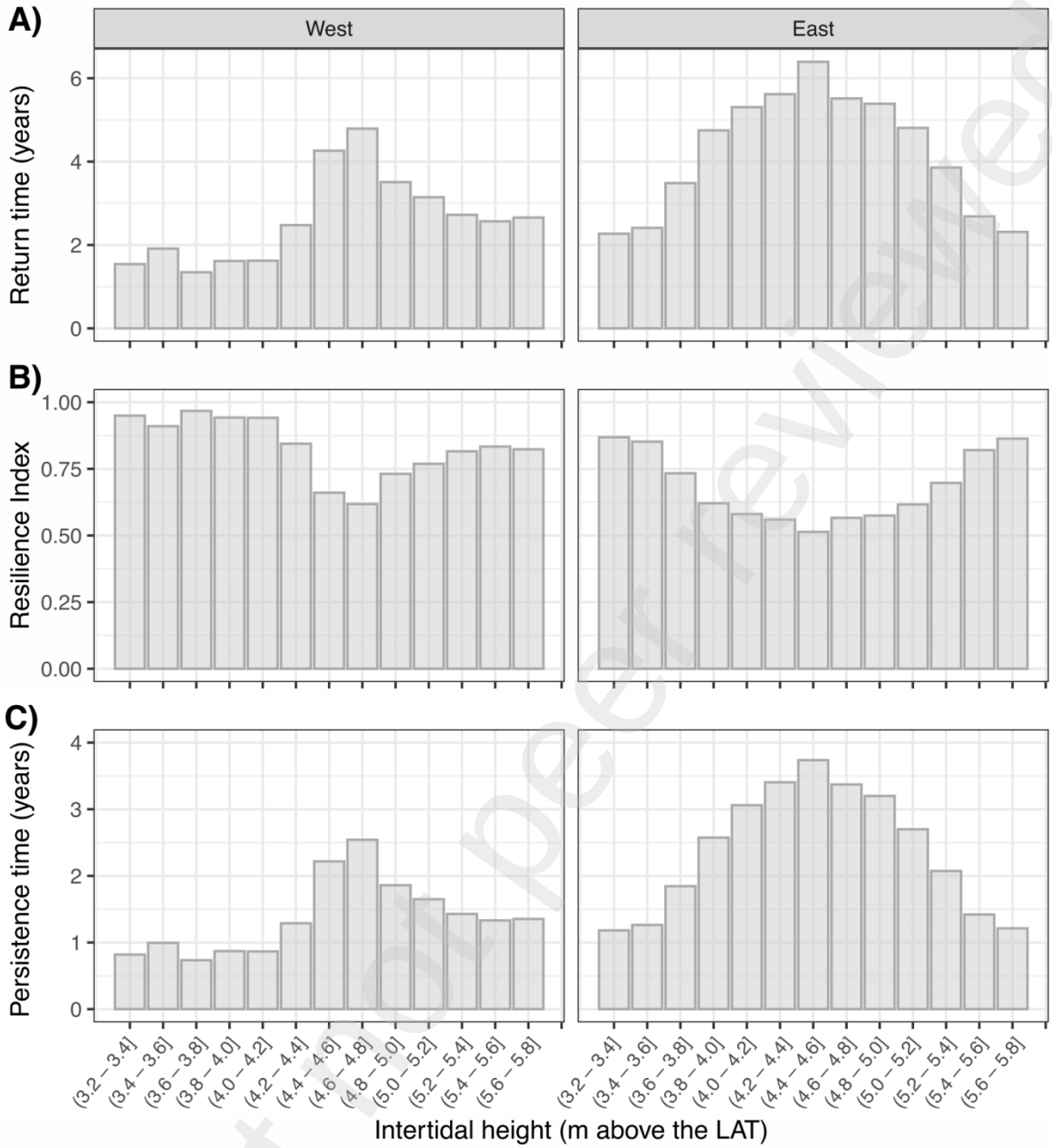

Figure 8. Predicted values along the intertidal height of the West and East shores, A) Return time (years) to equilibrium; B) resilience index (no unit; values between 0 and 1); C) persistence time (years) defined as the time during which 90% of the occupied cells remain occupied (quantile 90).

Supplementary 1

Table S1. Results of variance partitioning analyses of loss, persistence, and gain in the West and East rocky shores from "Le Petit Minou", France. The proportion explained represented in Figure 5 corresponds to the percentage representation of η^2.

shore	Variable	Df	Sum Sq	Mean Sq	F value	Pr(>F)	eta2	dynamics
West	intertidal height	2	8.6972	4.3486	143.03	1.4E-59	9.1	loss
West	orientation	11	0.4772	0.0434	1.43	1.5E-01	0.5	loss
West	slope	5	0.3299	0.0660	2.17	5.5E-02	0.3	loss
West	intertidal height:orientation	22	1.8250	0.0830	2.73	2.6E-05	1.9	loss
West	intertidal height:slope	10	1.0834	0.1083	3.56	1.0E-04	1.1	loss
West	orientation:slope	55	1.5521	0.0282	0.93	6.3E-01	1.6	loss
West	intertidal height:orientation:slope	110	5.1042	0.0464	1.53	4.5E-04	5.3	loss
West	residuals	2529	76.8895	0.0304	NA	NA	80.1	loss
shore	Variable	Df	Sum Sq	Mean Sq	F value	Pr(>F)	eta2	dynamics
West	intertidal height	2	9.3979	4.6990	224.04	2.6E-90	13.6	persistence
West	orientation	11	0.5011	0.0456	2.17	1.4E-02	0.7	persistence
West	slope	5	0.6452	0.1290	6.15	1.1E-05	0.9	persistence
West	intertidal height:orientation	22	1.3901	0.0632	3.01	3.1E-06	2.0	persistence
West	intertidal height:slope	10	0.8481	0.0848	4.04	1.6E-05	1.2	persistence
West	orientation:slope	55	0.9714	0.0177	0.84	7.9E-01	1.4	persistence
West	intertidal height:orientation:slope	110	2.2169	0.0202	0.96	6.0E-01	3.2	persistence
West	residuals	2529	53.0415	0.0210	NA	NA	76.9	persistence
shore	Variable	Df	Sum Sq	Mean Sq	F value	Pr(>F)	eta2	dynamics
West	intertidal height	2	0.0268	0.0134	124.20	3.5E-52	7.8	gain
West	orientation	11	0.0038	0.0003	3.18	2.7E-04	1.1	gain
West	slope	5	0.0108	0.0022	20.08	1.1E-19	3.2	gain
West	intertidal height:orientation	22	0.0060	0.0003	2.54	1.0E-04	1.8	gain
West	intertidal height:slope	10	0.0073	0.0007	6.75	1.9E-10	2.1	gain
West	orientation:slope	55	0.0048	0.0001	0.80	8.5E-01	1.4	gain
West	intertidal height:orientation:slope	110	0.0099	0.0001	0.83	9.0E-01	2.9	gain
West	residuals	2529	0.2731	0.0001	NA	NA	79.7	gain

shore	Variable	Df	Sum Sq	Mean Sq	F value	Pr(>F)	eta2	dynamics
East	intertidal height	2	57.0249	28.5125	1721.98	0.0E+00	53.6	loss
East	orientation	11	0.8421	0.0766	4.62	5.2E-07	0.8	loss
East	slope	5	0.3563	0.0713	4.30	6.7E-04	0.3	loss
East	intertidal height:orientation	22	0.5610	0.0255	1.54	5.2E-02	0.5	loss
East	intertidal height:slope	10	0.7792	0.0779	4.71	1.1E-06	0.7	loss
East	orientation:slope	55	1.8212	0.0331	2.00	2.1E-05	1.7	loss
East	intertidal height:orientation:slope	110	2.7239	0.0248	1.50	8.1E-04	2.6	loss
East	residuals	2559	42.3717	0.0166	NA	NA	39.8	loss
shore	Variable	Df	Sum Sq	Mean Sq	F value	Pr(>F)	eta2	dynamics
East	intertidal height	2	59.8353	29.9176	2067.45	0.0E+00	58.3	persistence
East	orientation	11	1.1222	0.1020	7.05	6.9E-12	1.1	persistence
East	slope	5	0.6046	0.1209	8.36	7.5E-08	0.6	persistence
East	intertidal height:orientation	22	0.4904	0.0223	1.54	5.2E-02	0.5	persistence
East	intertidal height:slope	10	0.5713	0.0571	3.95	2.3E-05	0.6	persistence
East	orientation:slope	55	1.4124	0.0257	1.77	4.3E-04	1.4	persistence
East	intertidal height:orientation:slope	110	1.6307	0.0148	1.02	4.1E-01	1.6	persistence
East	residuals	2559	37.0308	0.0145	NA	NA	36.1	persistence
shore	Variable	Df	Sum Sq	Mean Sq	F value	Pr(>F)	eta2	dynamics
East	intertidal height	2	0.0449	0.0224	390.36	1.1E-148	20.3	gain
East	orientation	11	0.0027	0.0002	4.28	2.4E-06	1.2	gain
East	slope	5	0.0092	0.0018	31.86	1.4E-31	4.1	gain
East	intertidal height:orientation	22	0.0024	0.0001	1.93	5.6E-03	1.1	gain
East	intertidal height:slope	10	0.0032	0.0003	5.55	3.2E-08	1.4	gain
East	orientation:slope	55	0.0055	0.0001	1.74	6.4E-04	2.5	gain
East	intertidal height:orientation:slope	110	0.0058	0.0001	0.92	7.1E-01	2.6	gain
East	residuals	2559	0.1470	0.0001	NA	NA	66.6	gain

824

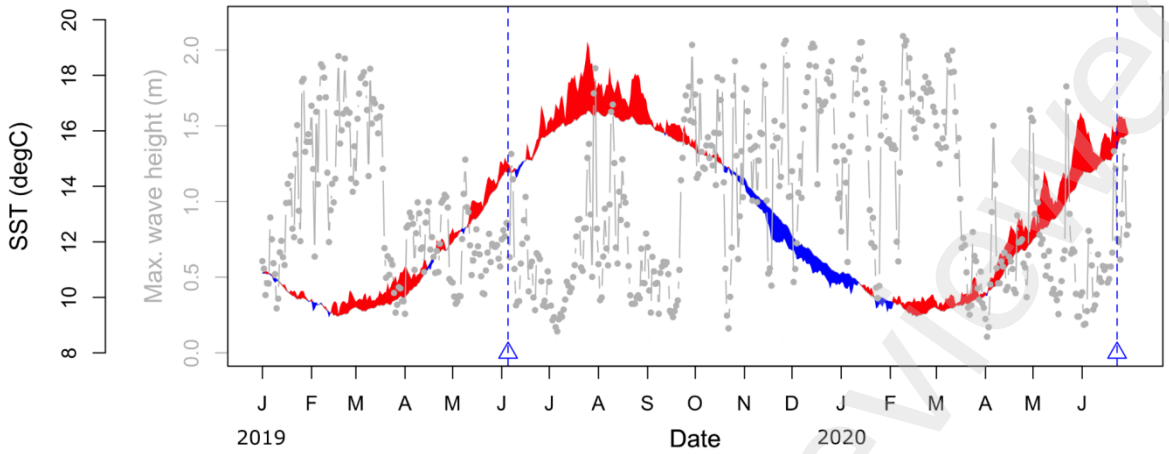

825

826 **Figure S1.** Daily dynamics of water temperature (black y-axis and continuous line) and
827 maximum wave height (grey y-axis and grey dots). The central black line represents the mean
828 water temperature from the historical period 2009-2018; red and blue fill indicate the positive
829 and negative difference of daily temperature against the historical mean, respectively. Blue
830 triangles indicate the date of drone surveys. The period of high temperature and wave height
831 occurred from late July to mid-August 2019.